

Electrochemical Stability of Platinum Nanoparticles Supported on N-Doped Hydrothermal Carbon Aerogels as Electrocatalysts for the Oxygen Reduction Reaction

Julian Martin,^[a, b, c] Julia Melke,^{*[a, b, c]} Christian Njel,^[d] Alexander Schökel,^[e] Jan Büttner,^[a, c, f] and Anna Fischer^{*,[a, b, c, f]}

Sustainable N-doped carbon aerogels were synthesized by a scalable hydrothermal approach using low-cost and abundant precursors such as glucose and ovalbumin. By adjusting the pyrolysis temperature (900–1500 °C), the surface chemistry, porosity and conductivity of these aerogels could be optimized for the design of Pt-based oxygen reduction reaction (ORR) catalysts with high Pt loading (40 wt% Pt) and improved stability. Pt nanoparticle deposition was realized by wet impregnation followed by thermal reduction and their size and distribution was found to strongly depend on the surface chemistry of the carbon aerogels. The catalysts' activities and stabilities, determined by rotating disc electrode measurements in HClO₄, were found to strongly depend on the pyrolysis

temperature of the N-doped carbon aerogel supports. While the mass activity decreased with increasing temperature, in line with a decreasing ECSA related to an increase in Pt nanoparticle size, the long-term stability of the catalysts, as revealed by accelerated stress tests for carbon support degradation (10,000 cycles), increased with increasing pyrolysis temperature, in line with increasing Pt nanoparticle sizes and increasing graphitization of the carbon aerogel supports. Most importantly, the catalyst derived from aerogels pyrolyzed at 1000 °C achieved a good compromise between activity and stability and revealed a superior ORR activity after the accelerated stress test in comparison to a commercially available Pt/C reference catalyst (40 wt% Pt).

Introduction

In polymer electrolyte fuel cells (PEMFC), composed of an anode and a cathode separated by a polymer electrolyte membrane, power is generated by the electrochemical oxidation of hydrogen (H₂) at the anode and the electrochemical reduction of oxygen (O₂), from air, at the cathode. In theory, the only reaction product is water (H₂O) in case catalysts are employed favoring a 4-electron transfer pathway. This technology thereby allows a clean production of electrical energy with respect to a sustainable future.^[1]

The most active and hence commercially employed electrocatalysts for PEMFCs are to date still based on Platinum-Group-Metal (PGM) nanoparticles (mostly platinum-based) supported on porous and conductive carbon materials.^[2] The catalytic activity for the oxygen reduction reaction (ORR) of carbon supported platinum nanoparticles has thereby been demonstrated to depend on particle size and inter-particle distance.^[3] Further it was shown, that the mass activity is maximized for platinum nanoparticles with sizes between 3 and 5 nm.^[4] The main limiting factor for such carbon supported platinum-based nanocatalysts is however their limited lifetime under operation, especially at the cathode side.^[2] Catalyst degradation processes

[a] J. Martin, Dr. J. Melke, J. Büttner, Prof. A. Fischer
Institute for Inorganic and Analytical Chemistry (IAAC)
University of Freiburg
Albertstr. 21
79104 Freiburg, Germany
E-mail: julia.melke@gmail.com
anna.fischer@ac.uni-freiburg.de

[b] J. Martin, Dr. J. Melke, Prof. A. Fischer
Freiburg Materials Research Center (FMF)
University of Freiburg
Stefan-Meier-Str. 21
79104 Freiburg, Germany


[c] J. Martin, Dr. J. Melke, J. Büttner, Prof. A. Fischer
Freiburg Center for Interactive Materials
and Bioinspired Technologies (FIT)
University of Freiburg
Georges-Köhler-Allee 105
79110 Freiburg, Germany

[d] Dr. C. Njel
Institute for Applied Materials – Energy Storage Systems (IAM-ESS)
Karlsruhe Institute of Technology Department
Hermann-von-Helmholtz-Platz 1
76344 Eggstein-Leopoldshafen,
Germany

[e] Dr. A. Schökel
Deutsches Elektronen-Synchrotron DESY
Notkestr. 85
22608 Hamburg, Germany

[f] J. Büttner, Prof. A. Fischer
Cluster of Excellence livMatS
University of Freiburg
79104 Freiburg, Germany

 Supporting information for this article is available on the WWW under <https://doi.org/10.1002/celec.202101162>

 © 2021 The Authors. ChemElectroChem published by Wiley-VCH GmbH. This is an open access article under the terms of the Creative Commons Attribution Non-Commercial NoDerivs License, which permits use and distribution in any medium, provided the original work is properly cited, the use is non-commercial and no modifications or adaptations are made.

include coalescence, dissolution and even detachment of platinum nanoparticles from the support, as well as electrochemical corrosion of the carbon support itself; all leading to a decrease of electrochemically active surface area (ECSA) of platinum.^[5,6]

To minimize these degradation processes, strategies such as advantageous nanostructuring^[7,8] and graphitization of the carbon support^[9] can be employed in order to favor high dispersion and physical confinement of the Pt-based catalyst nanoparticles as well as to increase support stability against carbon corrosion. In addition, improving the dispersion and surface attachment/anchorage of the Pt nanoparticles onto the carbon support can also improve the stability of the resulting catalyst. In that context, it was shown, that the presence of certain N-functional groups such as pyridinic functionalities can work as anchoring points for Pt atoms thereby improving the Pt dispersion and Pt nanoparticle resistance against agglomeration and coalescence.^[10–12] Furthermore, such N-containing functional groups can also have a positive effect on the ionomer distribution at the catalyst surface, an activity determining parameter for membrane-electrode-assemblies (MEA) in PEMFCs.^[13]

State-of-the-art carbon supports for automotive fuel cell applications are carbon blacks, e.g. Vulcan[®]XC-72R or Black Pearls[®] (Cabot Corporation) and Ketjenblack[®] (Nouryon Chemicals B. V.).^[14] Beyond these “conventional” carbon blacks, a large variety of different carbon supports, which meet the criteria of high surface area and porosity^[15] as well as sufficient conductivity and corrosion stability for ORR, are known in literature: nanostructured carbon materials, like carbon nanotubes,^[16–18] carbon nanofibers,^[19,20] carbon aerogels^[21,22] as well as mesoporous N-doped carbons^[7,13] have been demonstrated suitable supports for platinum(-alloy)/carbon catalysts with higher ORR activities and/or stability than conventional Pt/C catalysts.

An elegant and sustainable class of materials among existing carbon support materials are nitrogen-doped carbon aerogels produced via hydrothermal carbonization.^[23–25] Hydrothermal carbonization (HTC) is a process for the production of functional carbon materials starting from biomass or biomass-derivatives in a bio-refinery concept. Biomass or biomass-derivatives are thereby converted under pressure and elevated temperature in an aqueous environment into carbonaceous precursor materials. Pyrolysis under inert atmosphere of these precursor materials further induces carbonization and/or graphitization (depending on the pyrolysis temperature and type of precursor), thereby allowing to adjust the materials chemistry and properties, e.g. sp²-C content, conductivity, surface area, pore volume as well as surface functionalities.^[26] Applications of HTC-derived carbon materials range from heterogeneous catalysis,^[27–29] e.g. fuel conversion^[30–32] and electrocatalysis^[33,34] to energy storage.

A simple one-pot synthesis of nitrogen-doped hydrothermal carbon aerogels (N-HTC), synthesized from glucose in the presence of a protein (ovalbumin), was first reported by White et al.^[35] Due to the presence of ovalbumin, acting both as nitrogen source and as structure directing/surface stabilizing

agent during the hydrothermal carbonization process, a cross-linked filigree carbonaceous gel structure is formed. Careful drying of the gel by freeze-drying or CO₂-supercritical drying allows to remove the solvent in the gel yielding carbonaceous aerogels with coral like nanostructures. Wohlgemut et al. and Brun et al. tested similar types of N-HTC aerogel materials as platinum-free catalysts for the oxygen reduction reaction (ORR).^[36,37] Compared to commercial platinum-based catalysts, the activities and stabilities of these catalysts did however not achieve the required performance for PEMFC (acidic medium). However, these N-HTC aerogels showed improved performance (especially in alkaline medium) for the ORR compared to previously reported platinum-free electrocatalysts.

Despite their promising properties, such as high surface area, open porous structure and tunable N-surface chemistry, all important parameters possibly influencing the dispersion, particle size and stability of Pt-nanoparticles under electrochemical conditions, these types of biomass derived N-HTC aerogels have, to the best of our knowledge, so far not been investigated as support materials for Pt-based ORR electrocatalysts.

By taking advantage of the structural properties of these N-HTC aerogels combined with a thorough fine tuning by different thermal treatments of their surface chemistry, crystallinity, conductivity and wettability, we could develop Pt/N-HTC ORR electrocatalysts with high Pt loading (40 wt %) exhibiting improved long-term stability in acidic medium. The best Pt/N-HTC electrocatalyst designed thereby outperformed a commercial reference Pt/C electrocatalyst with the same Pt loading (Pt40/C, QuinTech) over 10,000 cycles accelerated stress test addressing carbon support corrosion.

Besides support design, we also thoroughly investigated platinum nanoparticle deposition onto these various N-HTC aerogels and systematically investigated the influence of morphology, surface area, pore and Pt nanoparticle characteristics on the electrocatalytic activity and stability of the resulting Pt/N-HTC electrocatalysts in order to identify activity and stability determining parameters in these catalysts. For this, the influence of various temperature treatments on the N-HTC supports were studied to develop a sustainable and simple method for fine tuning activity and stability determining parameters in these catalysts, such as N-HTC surface area, pore size, crystallinity and elemental composition (bulk and surface), as well as platinum nanoparticle size and dispersion.

Results and Discussion

Based on a synthesis route initially described by White et al.^[35] and adapted by some of us for Pd/N-HTC hydrogenation catalysts,^[26] nitrogen-doped carbonaceous aerogels (N-HTC) with coral like nanostructures were synthesized in a hydrothermal approach using glucose and ovalbumin as carbon precursor and nitrogen source/structure directing agent, respectively. To optimize the structural and physicochemical properties of these N-doped hydrothermal carbon aerogels (N-HTC) as supports for Pt-based ORR electrocatalysts, these

were pyrolyzed at different temperatures under inert atmosphere (900 °C, 1000 °C and 1500 °C). The resulting samples (N-HTC-PT, with PT being the pyrolysis temperature) were structurally characterized with regard to the pyrolysis temperature and changes in porosity, elemental composition, surface functionalization, crystallinity/structure and conductivity. Together, these crucial support properties influenced the Pt nanoparticle deposition/formation by wet impregnation/reduction as well as the ORR activity and stability of the resulting Pt/N-HTC-PT electrocatalysts.

Influence of carbonization/graphitization temperature

Synthesis of carbon materials was done starting from green and sustainable precursors, glucose and ovalbumin, in a hydrothermal carbonization approach. After careful drying of the raw product, to preserve the filigree structure, a second temper-

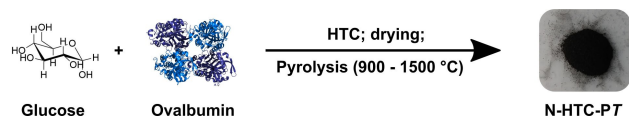


Figure 1. Synthesis scheme of the hydrothermal carbonization of glucose and ovalbumin to a nitrogen-doped hydrothermal carbon (N-HTC) support.

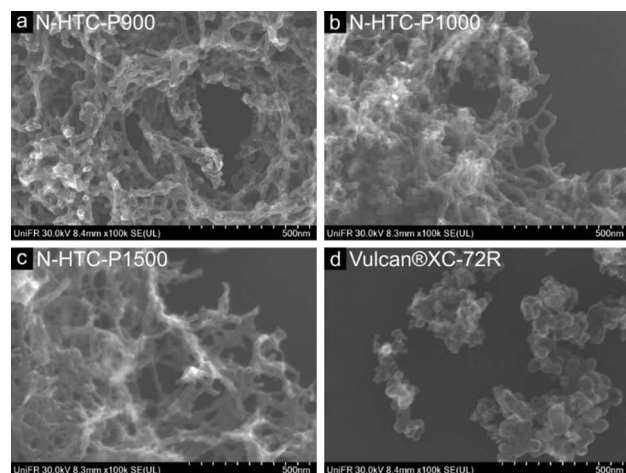


Figure 2. SEM micrographs of N-doped hydrothermal carbon aerogel supports treated at 900 °C (a), 1000 °C (b) and 1500 °C (c) and SEM micrograph of a commercial carbon support Vulcan®XC-72R (d).

ature step under inert atmosphere with different pyrolysis temperatures was performed (see Figure 1).

The morphology of the N-HTC-PT carbon support materials pyrolyzed at 900 °C, 1000 °C and 1500 °C, respectively, resembles a typical coral-like aerogel structure, as revealed by scanning electron microscopy; results, which are in line with the previous report of White et al.^[35] A detailed SEM characterization of the N-HTC-P900, P1000, P1500 is shown in Figure 2 and in the electronic supporting information (ESI, Figure S1). One can see an open porous aerogel structure with large macro- and mesopores composed of highly percolated coral like elongated carbon nanostructures. Advantageously, the morphology of the samples carbonized/graphitized at higher temperature remains unchanged by the temperature treatment. In contrast to a commercial carbon support often used in electrocatalysis, e.g. Vulcan®XC-72R (Figure 2d and ESI, Figure S1), which has a spherical particulate structure with a mean primary particle size of approximately 50 nm, the N-HTC materials itself has an open, mesoporous, percolated structure.

The porous properties of the N-HTC supports, including the Brunauer-Emmett-Teller (BET) surface area, pore volume and pore size distribution were determined via N₂-physisorption measurements at 77 K (see ESI, Figure S2). In good agreement with literature, the surface area first increases with pyrolysis temperature from 172 m²g⁻¹ for the crude product (i.e. after the hydrothermal carbonization) to 295 m²g⁻¹ and 305 m²g⁻¹ after pyrolysis at 900 °C and 1000 °C, respectively. For an even higher pyrolysis temperature, i.e. 1500 °C, the surface area decreases to 166 m²g⁻¹. All N-HTC samples exhibit a relatively similar pore size distribution (see ESI, Figure S3) in line with their morphology. The QSDTF computations show a very broad pore size distribution with a maximum at 1 nm located in the micropore range. Mostly mesopores between 2 and 30 nm contribute to the total pore volume, while the volume fraction of micropores is rather small (see ESI, Figure S4). With increasing pyrolysis temperature, the total pore volume first increases in line with BET surface area, while for higher pyrolysis temperature (> 1000 °C) most of the micropores are lost; presumably a result of a structural collapse.

The elemental bulk composition of the synthesized N-HTC materials was determined *via* elemental combustion analysis (C, H, N, S) and the results are summarized in Table 1. The oxygen content was calculated by assuming that the residual wt% after subtraction of the C, H, N, S wt% is ascribed to oxygen. For the crude N-HTC carbon the chemical bulk composition consists of

Table 1. Surface area, total, meso- and micropore volume of the N-doped hydrothermal carbon aerogels before and after temperature treatment at 900 °C, 1000 °C and 1500 °C (N-HTC-PT with T = pyrolysis temperature), as well as elemental composition determined *via* thermal combustion analysis.

Sample	^[a] S _{BET} /m ² g ⁻¹	^[b] V _{tot} /cm ³ g ⁻¹	V _{meso} /cm ³ g ⁻¹	V _{micro} /cm ³ g ⁻¹	C/wt%	N/wt%	H/wt%	S/wt%	^[c] O/wt%	C/N
N-HTC	172	0.61	0.58	0.03	60.4	5.4	5.8	0.9	27.5	11.2
N-HTC-P900	295	0.48	0.40	0.08	86.9	3.3	1.3	0.1	8.4	26.3
N-HTC-P1000	305	0.56	0.43	0.13	87.3	2.0	1.1	0.1	9.5	43.7
N-HTC-P1500	166	0.17	0.16	0.01	98.3	0.2	0.1	–	1.4	492.0
Vulcan®XC-72R	240	0.36	0.28	0.08	98.1	–	–	0.4	1.5	–

[a] The surface area was determined with use of the Brunauer-Emmett-Teller (BET) theory. [b] Pore Volumes were calculated using quenched solid density functional theory (QSDFT). The micropore fraction < 2 nm. [c] The residual wt% after subtraction of the C, H, N, S wt% was ascribed to oxygen.

60 wt% carbon, more than 5 wt% of nitrogen and nearly 30 wt% of oxygen. While for the synthesized samples at 900 °C and 1000 °C a considerable amount of nitrogen functional groups (3.3 wt% and 2.0 wt%, respectively) is still present, there is almost no nitrogen found in the sample pyrolyzed at 1500 °C and the material is composed of > 98 wt% of carbon.

The surface composition of the N-HTC-PT samples was further investigated by XPS (see Table 2). Survey XPS spectra (Figure 3a) revealed the presence of three main elements including carbon (C1s), oxygen (O1s), and nitrogen (N1s) as well as some minor traces of sulfur (S2p, see ESI Figure S5). In line with the results obtained from elemental analysis, the increase in pyrolysis temperature (from 900 °C to 1500 °C) reduces the amount of nitrogen and oxygen also at the surface of the N-HTC materials. Similar behavior has been observed for PANI-derived mesoporous nitrogen doped carbon nanospheres (MPNC) pyrolyzed at similar temperatures.^[38] Figure 3b shows the C1s detail spectra for Vulcan®XC-72R and for the N-HTC-PT samples carbonized at different temperatures. The C1s spectra can be fitted with five peaks each. The asymmetric shape of the C1s peak at 284.5 eV (violet component in Figure 3b) corresponds to the C=C environment with sp²-hybridization.^[39] The C2 narrow peak at 285 eV can be assigned to sp³-hybridized carbon (C-C/C-H).^[39] The peak around 286.5 eV (C3, green peak) was attributed to C-O and/or C-N (pyrolic) environments. The peak centered at 288.6 eV (C4, blue peak) can be ascribed to a mix of carbon environments including C=N (pyridinic), N-C=O and C=O functionalities.^[35,40] Finally the C5 peak (pink component) at around 291 eV was attributed to π-π* shake-up contributions. This satellite corresponds to the excitation of the

π-π* transition by the outgoing photoelectron from unsaturated carbons in C=C double bonds.^[41]

In line with the results from elemental analysis, one can see that for increasing pyrolysis temperature, the C2, C3, C4 and C5 contributions decrease until they nearly completely disappear for the highest pyrolysis temperature of 1500 °C, indicating the defunctionalization of the N-HTC-PT surface for increasing pyrolysis temperatures.

To gain a more differentiated picture of the N-HTC-PT surface, the O1s and N1s spectra were also analyzed.

The O1s spectra (Figure 3c) were fitted by three contributions accounting for oxygenated species present at the N-HTC surface. The peak observed at 530.6 eV (O1, purple component) was attributed to N-C=O species, while the other two peaks (O2 and O3, dark and light blue) at 532.5 eV and 536 eV were attributed to the O=C/C-OH environment of oxygen (O2, dark blue component),^[42] and the presence of surface adsorbed water molecules (O3, light blue component), respectively.^[43] What can clearly be seen, is that the O1s contribution, related to N-C=O environments, is disappearing for increasing pyrolysis temperatures; result, which is in line with the C1s data and the loss of N observed in elemental analysis. This is further confirmed by looking at the N1s spectra presented in Figure 3d. While the peak at 398.3 eV (N1, light green) is attributed to N=C environments of pyridinic nitrogen, the peak centered at 401 eV (N2, dark blue) is attributed to quaternary nitrogen.^[44] Another peak centered at 404 eV (N3, dark green) can be assigned to various oxidized nitrogen configurations like pyridine-N-oxide.^[45] In line with the C1s and O1s spectra discussed previously, one can again see a defunctionalization of the N-HTC surface with increasing pyrolysis temperature (the amount

Table 2. XPS results of N-HTC-PT samples and Vulcan®XC-72R reference carbon support.

Sample	C/at%	N/at%	O/at%	S/at%
N-HTC-P900	93.0	3.5	3.4	0.1
N-HTC-P1000	95.0	1.8	3.1	0.1
N-HTC-P1500	97.4	0.9	1.7	-
Vulcan®XC-72R	99.1	-	0.6	0.3

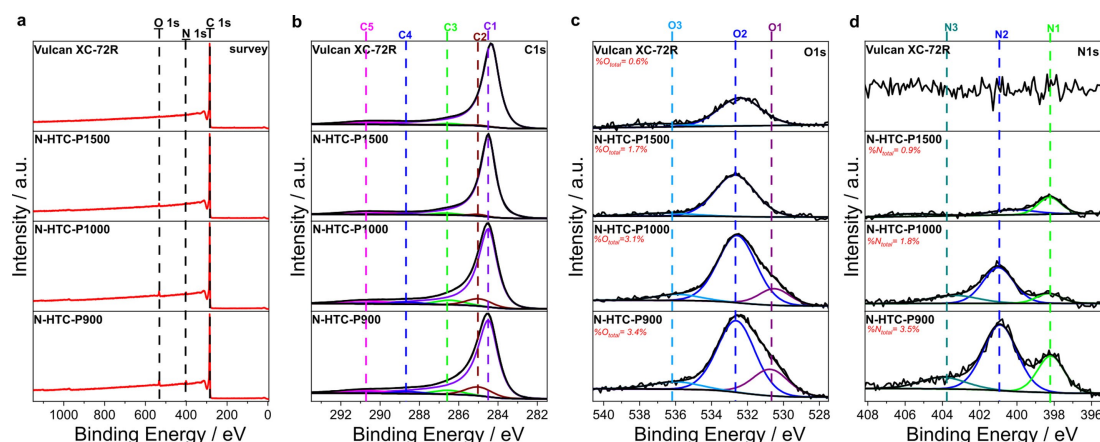


Figure 3. Survey (a), C1s (b) and O1s (c), and N1s (d) XPS spectra of N-HTC-PT samples at different temperature (900 °C, 1000 °C and 1500 °C, respectively) and Vulcan®XC-72R. The S2p detail spectrum is shown in the ESI.

of nitrogen left on the N-HTC surface is below 1 at%, with pyridinic nitrogen being the most stable nitrogen functionality at 1500 °C; result which is in line with the NEXAFS results (*vide infra*).

For comparison a commercially available reference carbon material, namely Vulcan®XC-72R, was also analyzed. The survey scan revealed a much higher carbon surface composition (99.1 at%) when compared to the N-HTC-PT materials (93.0 at%, 95.0 at% and 97.4 at% for $T=900$, 1000 and 1500 °C) and in line a lower amount of heteroatoms such as O (0.6 at%) and S (0.3 at%). Notably the Vulcan®XC-72R did not feature any N on its surface.

Further investigation of the surface chemistry of the N-HTC supports was done by Near-edge X-ray absorption fine structure spectroscopy (NEXAFS) (Figure 4). By analyzing the C K-edge (Figure 4a), an insight into the sp^2 -C content of the materials can be obtained.^[7,46] Highly ordered pyrolytic graphite (HOPG) served as reference material containing 100 at% of sp^2 -C carbon. The spectrum of HOPG shows the typical π^* resonance

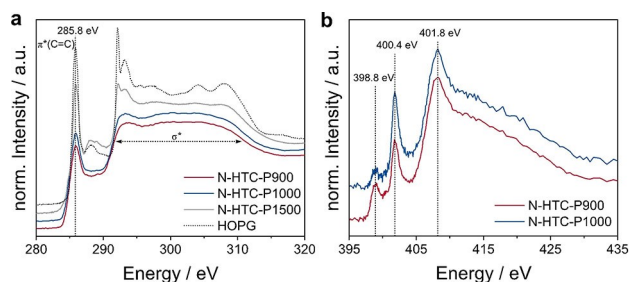


Figure 4. NEXAFS spectra C K-edge (a) and N K-edge (b) of N-HTC-PT samples pyrolyzed at different temperatures $T=900$, 1000, 1500 °C as well as of highly ordered pyrolytic graphite (HOPG).

at 285.8 eV ($C1s \rightarrow \pi^*$), characterizing the $C=C$ bond in the π -conjugated C-ring system of graphite.^[47] Additionally, above 292 eV, σ^* resonances ($C1s \rightarrow \sigma^*$) at 292.5, 297.8, 303.5, and 307.5 eV are visible.^[48] For the N-HTC-PT materials pyrolyzed at $T=900$ and 1000 °C the π^* transition (258.8 eV) is clearly visible, but with a smaller relative intensity, compared to HOPG. For the higher graphitized sample N-HTC-P1500, in addition to the π^* transition (258.8 eV), the fine structure between 292 eV and 310 eV (σ^* resonances) is more pronounced which indicates a higher sp^2 -C content. By correlating the π^* peak intensities of the N-HTC-PT materials with the π^* peak intensity of HOPG, the sp^2 -C content accounts for 64, 67 and 92 at% for N-HTC-P900, N-HTC-P1000 and N-HTC-P1500, respectively. This demonstrates as expected an increase of the sp^2 -C content with increasing carbonization temperature in the N-HTCs and is in line with previously reported PANI-derived carbons.^[38] For Vulcan®XC-72R an sp^2 -C content of 80 at% was determined and by analyzing the N K-edge NEXAFS spectra (Figure 4b) of the N-HTC-PT samples N-HTC-P900 and N-HTC-P1000 (containing nitrogen groups, as proven by EA and XPS) the type of N-functionalities was determined. The peaks at 398.8 eV, 400.4 eV and 401.8 eV can be assigned to pyridinic, amino and pyrrolic and/or graphitic (quaternary) type N-groups, respectively.^[49] Thereby, the relative intensity of the peak at 401.8 eV attributed to graphitic N-groups is higher for the sample pyrolyzed at 1000 °C than for the sample pyrolyzed at 900 °C, demonstrating the prevalence of graphitic N for higher temperature as this type of N is most stable,^[7] result, which is in line with the XPS results (*vide supra*).

Visualization of the carbon microstructure was done by HR-TEM (see Figure 5). For the N-HTC temperature series (Figure 5a–c) an increase of crystallinity, i.e. an increase in

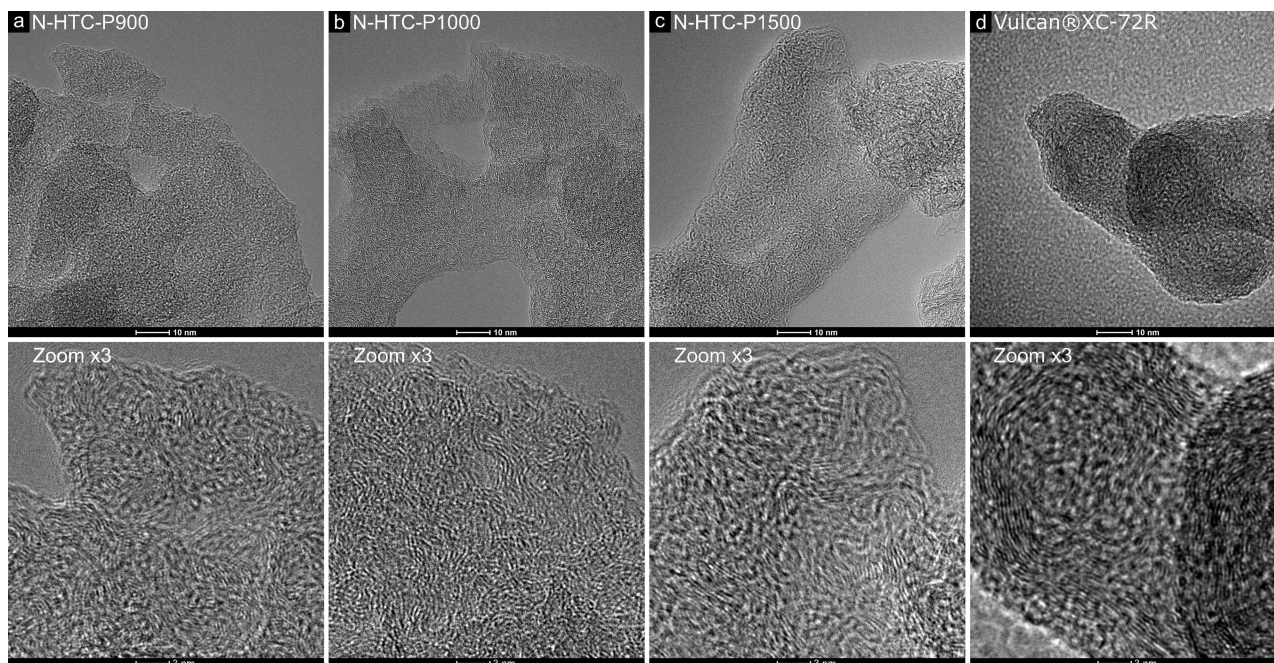


Figure 5. TEM micrographs of N-HTC-PT supports pyrolyzed at different temperatures $T=900$ (a), 1000 (b), 1500 °C (c) and of a commercial Vulcan®XC-72R reference support (d).

extension and stacking of graphene-like planes, is clearly visible for higher pyrolysis temperatures. In comparison, the Vulcan®XC-72R material (Figure 5d) evidences a comparable extension and stacking of graphene-like planes as observed for the N-HTC-P1500 sample. These findings are in line with the NEXAFS results (*vide supra*).

Further investigations by Raman spectroscopy corroborate these findings (Figure 6 and ESI, Figure S6 and S7). For all samples a broadened Raman signal is observed when compared to graphite, indicating larger amounts of amorphous carbon and the presence of defects in the carbon structure.^[50] Only for the N-HTC-PT sample prepared at a higher pyrolysis temperature of 1500 °C a clear difference in the Raman spectra can be observed when compared to the N-HTC-PT samples pyrolyzed at lower temperatures (i.e. 900 and 1000 °C) and Vulcan®XC-72R. The D(1)-band (1345 cm⁻¹) and G band (1580 cm⁻¹) are sharpened and the 2D-band (2400–3000 cm⁻¹), assigned to a second-order Raman band, indicate a higher graphitization degree.^[51,52]

The Raman spectra of the N-HTC-PT materials were fitted assuming a 5-band model with mixed Gaussian/Lorentzian peaks (see ESI, Figure S4). For highly disordered carbon nano-materials, additionally, to the G-band (lattice vibration mode of E_{2g} symmetry of the perfect hexagonal lattice of graphite) and D1-band (vibration mode of A_{1g} symmetry of disordered graph-

itic lattice) three other D-bands at 1210 cm⁻¹ (D4), 1530 cm⁻¹ (D3) and 1604 cm⁻¹ (D2) can be denoted.^[52] Even though, a quantitative analysis of the amorphous content and in-plane crystallite length is difficult,^[52-54] the fit results (see ESI, Figure S5) show, that for the N-HTC-PT materials the deconvoluted peak areas of the D3- and D4-band, assigned to amorphous carbon^[52] and trans-polyacetylene-like chains at layer edges,^[54,55] respectively, decreases, whereas the D1-, D2- and G-band peak area increases for a higher carbonization/graphitization.

X-Ray diffraction was used to evaluate the crystallinity of the N-HTC-PT materials (see Figure 7a). For all N-HTC-PT materials, three features can be seen in the XRD patterns, which can be attributed to the (002), (100)/(101) and (110) reflections of hexagonal graphite (P6₃/mmc). With increasing pyrolysis temperature these reflections become more pronounced and slightly sharper, showing an increase in crystallinity of the carbon phase, especially for the N-HTC-P1500 sample.

To further investigate the crystallinity/ordering in the samples in a more quantitative manner, X-ray scattering measurements were performed, and atomic pair distribution functions G(r) derived (Figure 7c). For all carbon samples, oscillations are observed within the pair distribution functions with maxima at r(Å) values close to the values expected for interatomic distances in hexagonal graphite. Moreover, the extension of these oscillations is increasing with increasing

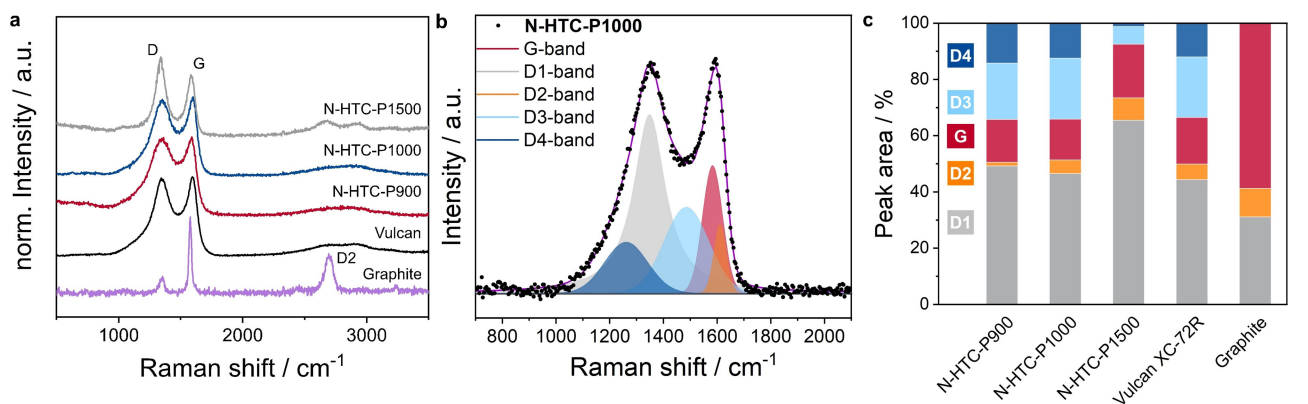


Figure 6. Raman spectra (a) of the N-HTC-PT materials, Vulcan®XC-72R and Graphite as reference. The spectra were fitted with five bands, as described previously and exemplarily shown for N-HTC-P1000 (b). The fitting results are shown in (c) and additional fitting results are presented in ESI.

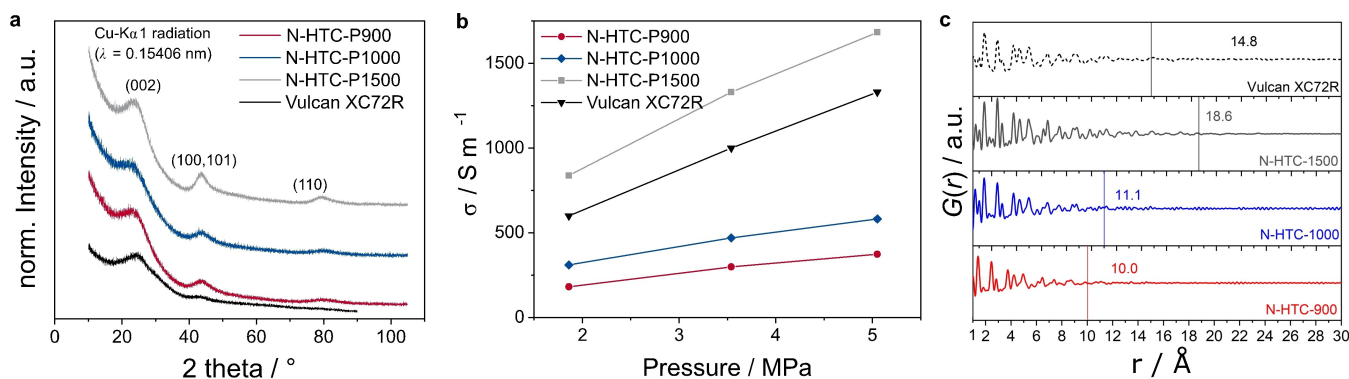


Figure 7. Powder diffraction measurements of the N-HTC-PT samples and Vulcan®XC-72R (a), pressure-dependent electrical conductivity of the various carbon materials (b) and radial distribution functions (c).

pyrolysis/graphitization temperature and reflects the extension of the graphitic / ordered crystallites / domains which is found to account for 10.0, 11.1 and 18.6 Å for N-HTC-P900, N-HTC-P1000, N-HTC-P1500, respectively. Hence, for the N-HTCs, the size of the graphitic crystallites was found to increase with increasing pyrolysis/graphitization temperature in accordance with the HR-TEM and Raman spectroscopy data presented previously (*vide supra*). For Vulcan®XC-72R an extension of 14.8 Å, in between the values found for N-HTC-P1000 and N-HTC-P1500, was determined.

The increase in graphitization and/or sp^2 -C content in the N-HTC materials cannot only be seen in the microstructure of the supports but also influences macroscopic properties, like the electrical conductivity. Determination of the electrical conductivity was performed under various degrees of powder compression (governed by different loads, see experimental part for details), as the conductivity of such powders is highly dependent on the contact/percolation existing between the powder particles and the settled apparent density.^[56] Therefore, the electrical conductivity increases with increasing load and hence compressive pressure.^[57] For the synthesized N-HTC-PT samples and the Vulcan®XC-72R material the electrical conductivity was found to increase in the order N-HTC-P900 < N-HTC-P1000 < Vulcan®XC-72R < N-HTC-P1500 (see Figure 7b). These findings match with the increasing sp^2 -C content and the increasing crystallite size determined by NEXAFS and total scattering analysis (*vide supra*).

Platinum nanoparticle deposition

Platinum nanoparticles (with a Pt mass loading of approx. 40 wt%) were deposited onto the N-HTC-PT samples pyrolyzed at different temperatures with $T = 900, 1000$ and 1500 °C via wet impregnation/reduction (see Table 3). For this purpose, a platinum (IV) precursor solution was impregnated onto the N-HTC-PT support followed by reduction in hydrogen gas at 100 °C (for details see experimental part).

The wet deposition/reduction process leads to crystalline Platinum nanoparticles (fcc lattice, see Table S11 in the ESI for refined parameters), as determined by X-ray diffraction (ESI, Figure S10). All samples consist of very small and finely distributed Pt nanoparticles on the N-HTC-PT supports along with larger agglomerates, as determined from XRD and TEM measurements (Figure 8 and ESI, Figure S8). The size of the platinum nanoparticles formed on the N-HTC-PT supports with $T = 900, 100$ and 1500 °C increases with increasing pyrolysis

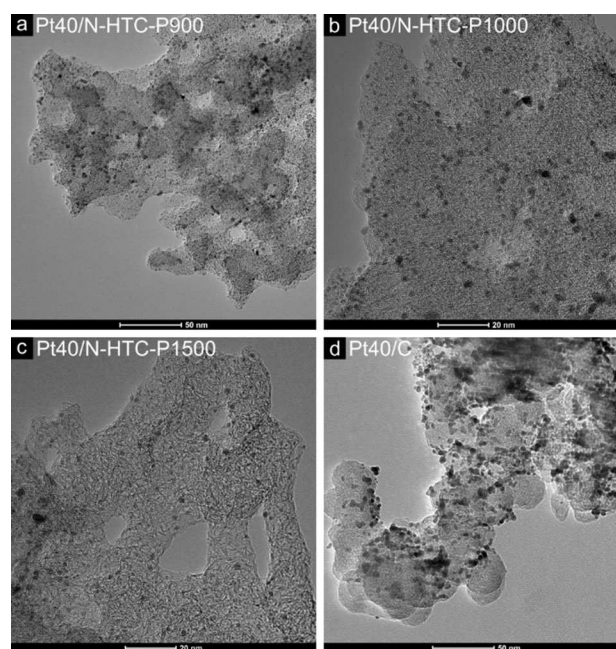


Figure 8. TEM micrographs of the different Pt-based catalysts analyzed in this study: Pt40/N-HTC-P900 (a), Pt40/N-HTC-P1000 (b), Pt40/N-HTC-P1500 (c) and Pt40/C (d).

temperature from (2.4 ± 0.6) nm over (2.9 ± 1.0) nm to (3.4 ± 0.9) nm, respectively, as determined via TEM (as summarized in Table 3 < tabr3). Rietveld refinement of the XRD pattern was performed to determine the Pt crystallite size within all samples. The respective diffractograms were analyzed by assuming the presence of two platinum phases with distinct crystallite sizes, meaning a bimodal distribution of the Pt nanoparticles (see ESI, Figure S10). Consistent with the TEM evaluation, the Rietveld refinement results show an increase in Pt crystallite size with increasing pyrolysis temperature of the respective carbon support (see Table 3), with the smallest particles obtained for the N-HTC-P900 sample and the largest particles obtained for the N-HTC-P1500 sample. As in all cases, the same reduction temperature was used and similar surface areas and pore volumes are given for the different N-HTC-PT samples, we attribute the stabilization of smaller Pt nanoparticle sizes on the N-HTC-P900 support to the higher N-content (of 3.3 wt%), presumably resulting in a better anchoring of the Pt precursor as well as of the formed Pt nuclei and final Pt nanoparticles after reduction. In comparison to a commercially available Pt40/C reference fuel cell catalyst with a Pt loading of 40 wt%

Table 3. Properties (BET surface area, pore volume and Nitrogen content) of the carbon support materials and respective Platinum mass loading (determined by TGA) and Pt NP sizes (determined via TEM) as well as Pt crystallite sizes (determined by XRD) with atomic fraction of the phase of the Pt40/N-HTC-PT catalysts (with $T = 900, 1000$ and 1500 °C) and a commercial Pt40/C reference catalyst.

Sample	$S_{\text{BET}}/\text{m}^2\text{g}^{-1}$	$V_{\text{tot}}/\text{cm}^3\text{g}^{-1}$	$N_{\text{EA}}/\text{wt}\%$	$L_{\text{P}}/\text{wt}\%$	d_{TEM}/nm	$d_{\text{XRD}\#1}/\text{nm}$		$d_{\text{XRD}\#2}/\text{nm}$	
Pt40/N-HTC-P900	295	0.48	3.3	42.1	2.4 ± 0.6	2.9	67 %	6.7	33 %
Pt40/N-HTC-P1000	305	0.56	2.0	39.7	2.9 ± 1.0	4.0	68 %	8.2	32 %
Pt40/N-HTC-P1500	166	0.17	0.2	40.0	3.4 ± 0.9	4.4	69 %	8.8	31 %
Pt40/C	240	0.36	–	41.5	3.1 ± 0.7	2.4	100 %	–	–

supported on Vulcan (see ESI, Figure S9) and Pt nanoparticle sizes of (3.1 ± 0.7) nm and crystallite sizes of 2.4 nm (determined via Rietveld refinement), the determined Pt particle/crystallite sizes for the Pt/N-HTC-PT materials are in a similar range. However, while the Pt nanoparticles on the Pt/N-HTC-PT are bimodal and also form in some cases larger agglomerates, the Pt nanoparticles in the Pt40/C reference catalyst feature a monomodal crystallite size distribution as determined by XRD.

Performance in electrocatalytic oxygen reduction – activity and stability

Electrochemical evaluation of the oxygen reduction reaction (ORR) activity and stability of the three Pt40/N-HTC-PT catalysts with $T=900, 1000$ and 1500 °C was carried out with a rotating disc electrode (RDE) setup with cyclic voltammetry and linear sweep voltammetry measurements for all three prepared catalysts and compared to the commercially available Pt/C reference catalyst (40 wt%, Pt on Vulcan, QuinTech). To simulate the long-term stability, especially in terms of carbon corrosion, accelerated stress tests (AST) were applied and the ORR activity was determined initially and after potential cycling. The AST were adapted from the Department of Energy (DoE) fuel cell targets and are designed to evaluate the corrosion of catalyst supports.^[58] The recorded CVs and LSVs are summarized together with the determined activities (mass and specific) before and after AST cycling in Figure 9. The CVs show the characteristic features for platinum in aqueous 0.1 M HClO₄ electrolyte (pH 1) for all tested samples. The electrochemical active surface area (ECSA) for the Pt40/N-HTC-PT catalysts

decreases with increasing pyrolysis temperature of the support from $51 \text{ m}^2 \text{g}_{\text{Pt}}^{-1}$ for Pt40/N-HTC-P900 to $35 \text{ m}^2 \text{g}_{\text{Pt}}^{-1}$ and $26 \text{ m}^2 \text{g}_{\text{Pt}}^{-1}$ for Pt40/N-HTC-P1000 and Pt40/N-HTC-P1500, respectively. The decrease in ECSA can be explained by the increase in Pt nanoparticle/nanocrystallite size determined by TEM and XRD (*vide supra*) as well as by the appearance of larger agglomerates, both reducing the catalytically active surface area. The ECSA of the commercially available Pt40/C reference catalyst ($46 \text{ m}^2 \text{g}_{\text{Pt}}^{-1}$) is somewhat smaller than the ECSA of the Pt40/N-HTC-P900 electrocatalysts ($51 \text{ m}^2 \text{g}_{\text{Pt}}^{-1}$), which, despite the smaller crystallite size determined by XRD and equivalent particle size (determined by TEM), is in line with the Pt nanoparticle agglomerates (seen in TEM) and the respective surface area of the support.

The onset potential of all catalyst (see experimental part) was determined to be at 0.95 V vs. RHE. The resulting ORR activities (specific and mass activity) were determined at 0.9 V vs. RHE (see experimental part for methodology). In terms of specific activity (SA), which is the kinetic ORR current normalized to the ECSA, in other words the ORR activity normalized to the real surface area of the Pt nanoparticles, one can see that it increases with increasing pyrolysis temperature of the N-HTC-PT supports (Figure 9). The SA thereby increases from $0.29 \text{ mA/cm}^2_{\text{Pt}}$ for Pt40/N-HTC-P900 over $0.31 \text{ mA/cm}^2_{\text{Pt}}$ for Pt40/N-HTC-P1000 to $0.35 \text{ mA/cm}^2_{\text{Pt}}$ for Pt40/N-HTC-P1500. As for increasing pyrolysis temperature the Pt nanoparticle sizes were found to increase, we can correlate the increase in specific activity in the Pt40/N-HTC-PT series with the increase in particle size. This result is in line with the ORR specific activity being particle-size-dependent and increasing with particle size.^[3,4,59] Previous studies showed, that smaller Pt nanoparticles have a

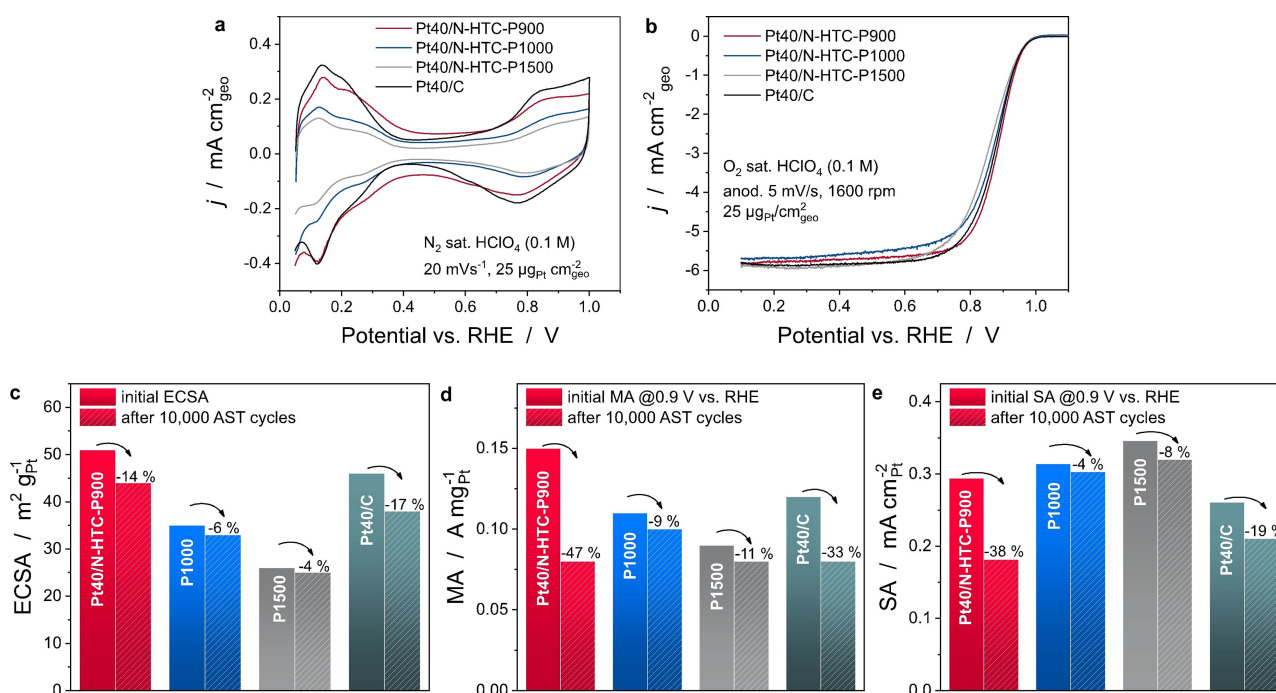


Figure 9. CVs (a), LSVs (b) as well as derived electrochemical active surface area (ECSA) (c), mass activity (MA) (d) and specific activity (e) for all three Pt40/N-HTC-PT electrocatalysts with $T=900, 1000$ and 1500 °C and a Pt40/C reference catalyst from QuinTech before and after AST cycling.

higher ECSA, as shown before, but a lower SA, which is increasing for larger particles. From all investigated catalysts, the Pt40/C reference catalyst has the lowest specific activity ($0.26 \text{ mA/cm}^2_{\text{Pt}}$), which can be attributed to the fact that all the Pt40/N-HTC-PT catalysts have larger particle / crystallite sizes. In addition, a superimposing positive influence of the N-content on the specific activity can be a plausible explanation for the observed increase in specific activity, at least for the Pt40/N-HTC-P900 and Pt40/N-HTC-P1000 samples, which have a non-negligible amount of N at the samples surface. However, all in all, the specific activities of the investigated catalysts are in a similar range.

The mass activity determined at 0.9 V vs. RHE (see experimental part for methodology) decreases with increasing pyrolysis temperature of the support, i.e. from $0.15 \text{ A mg}_{\text{Pt}}^{-1}$ for Pt40/N-HTC-P900 over $0.11 \text{ A mg}_{\text{Pt}}^{-1}$ for Pt40/N-HTC-P1000 to $0.09 \text{ A mg}_{\text{Pt}}^{-1}$ for Pt40/N-HTC-P1500; results, which are in line with the decreasing ECSA values and increasing particle/crystallite sizes observed previously. In comparison, the commercially available Pt40/C catalyst from QuinTech reached a mass activity of $0.12 \text{ A mg}_{\text{Pt}}^{-1}$. As such the best performing catalyst among the Pt40/N-HTC-PT catalysts (in terms of mass activity), i.e. Pt40/N-HTC-P900, has a higher ORR mass activity than the commercially available reference catalyst in acidic media. We attribute this increased mass activity to (i) the higher ECSA of the Pt40/N-HTC-P900 catalyst, i.e. a higher Pt dispersion and (ii) to the high N-content of the N-HTC-P900 carbon support. More precisely, the Nitrogen-doping has an undeniable role in the formation and size-control of the Pt nanoparticles formed on the N-HTC-PT supports, ensuring a more homogenous distribution of the platinum-salt precursor and hence “anchoring” on the support. As such, the N-content governs the obtained nanoparticle size and thereby “indirectly” the initial ORR activity of the Pt40/N-HTC-PT catalysts. In addition, a direct electronic effect of the N-functionalities on carbon supports on the ORR activity of Pt–N–C catalysts^[53, 60–62] cannot be excluded and may also contribute to the observed higher initial mass activity.

To investigate the stability of the Pt40/N-HTC-PT catalysts in comparison to the Pt40/C reference catalyst, accelerated stress tests (AST) designed for support corrosion (following DoE protocols) were performed and the ECSA and ORR activity (MA and SA) were evaluated. After 10,000 potential cycles (between 1 and 1.5 V vs. RHE in N_2 saturated electrolyte, support corrosion AST) the Pt40/N-HTC-PT catalysts showed an improved stability in terms of ECSA, mass activity and specific activity compared to the Pt40/C reference catalyst (Figure 9). While the ECSA of the Pt40/C reference catalyst decreased by 17%, the ECSA of the Pt40/N-HTC-P900 decreased by only 14%. An even smaller decrease of ECSA of only 6% and 4% was observed for the Pt40/N-HTC-P1000 and Pt40/N-HTC-P1500 catalysts, exhibiting a higher graphitization of the carbon support. These results clearly evidence the beneficial effect of the support graphitization on the electrochemical stability. In terms of mass activity, a severe decrease by 33% was observed for the Pt40/C reference catalyst. While an even more pronounced decrease by 47% was observed for the Pt40/N-

HTC-P900 catalyst, the higher graphitized Pt40/N-HTC-P1000 and Pt40/N-HTC-P1500 catalysts hardly lost any activity (< 10%). Similar results are obtained in terms of specific activities. To summarize, the comparison of ECSA and ORR activity values (mass and specific) before and after AST clearly demonstrate that the higher graphitization of the N-HTC-PT supports contributes to an increased long-term stability of the Pt-based catalysts, probably as a result of a higher support stability against carbon corrosion. These results are in line with previous works, demonstrating an improved electrochemical corrosion-resistance of carbon materials, like Vulcan®XC-72R and Ketjen-black, with a higher graphitization or temperature treatment.^[63,64] It is also important to note, that catalysts with a smaller ECSA and larger Pt nanoparticle/crystallite sizes are more stable against degradation,^[65,66] which is also the case for the samples studied here. The increased stability of the Pt40/N-HTC-PT with $T > 900^\circ\text{C}$ is therefore most probably a combination of particle size effects and support effects, i.e. increasing Pt nanoparticle/crystallite sizes as well as increased graphitization, respectively. Correlations between activity and stability and particle size, ECSA as well as N-content, BET surface area of the supports and carbonization/graphitization on the ORR activity and stability are summarized in correlation plots in the ESI (Figure S11 and Figure S12). In any case, while the Pt40/N-HTC-P900 catalyst outperforms the Pt40/C reference catalyst in terms of mass and specific activity, the more graphitized catalysts Pt40/N-HTC-P1000 and Pt40/N-HTC-P1500 outperform the Pt40/C reference catalyst in terms of stability, with Pt40/N-HTC-P1000 achieving a good balance between both beginning of life activity and long-term stability. As such, by fine-tuning the physicochemical properties of our N-HTC-PT aerogel supports (by high temperature pyrolysis), we could engineer both the Pt nanoparticle size distribution as well as the corrosion stability of our supports and thereby fine-tune the ORR activity as well as stability of the resulting Pt40/N-HTC-PT electrocatalysts. This result is especially significant, since we are working with rather high Pt loadings on the carbon support (40 wt%), relevant for real fuel cell applications.^[67]

Conclusion

In this work we synthesized and optimized nitrogen-doped hydrothermal carbon aerogels (N-HTC) as “sustainable” support materials for the design of platinum-based oxygen reduction (ORR) electrocatalysts in acidic media. The aerogel synthesis was based on an easy one-pot hydrothermal synthesis route, starting from green precursors such as glucose and ovalbumin, followed by a subsequent carbonization step, allowing to fine tune the physicochemical properties of the carbon materials in terms of their elemental/surface composition, porosity, carbonization/graphitization and conductivity. Platinum nanoparticles (40 wt%) were deposited by simple wet impregnation/reduction and it was revealed that the support N-content as well as surface area had a major influence on the Pt nanoparticle size and dispersion in/on the support. The Pt40/N-HTC-PT catalysts were evaluated by RDE towards their activity and stability (in

carbon corrosion accelerated stress tests (AST)) for the ORR in acidic media (i.e. 0.1 M HClO₄). We could thereby reveal that (i) a higher N-content and smaller particle size is beneficial for the mass activity of the catalyst while (ii) a higher graphitization is required for extended stability. After optimization, the newly designed Pt₄₀/N-HTC-P1000 catalyst exhibited a comparable mass activity to a commercial Pt₄₀/C (Pt 40 wt% on Vulcan, QuinTech) reference catalyst (0.11 A mg_{Pt}⁻¹ vs. 0.12 A mg_{Pt}⁻¹, respectively), but outperformed the reference catalyst in long term stability (0.10 A mg_{Pt}⁻¹ vs. 0.08 A mg_{Pt}⁻¹ after AST, respectively). While the Pt₄₀/C catalyst lost more than 30% in terms of ECSA, mass activity and specific activity during AST, the Pt₄₀/N-HTC-P1000 catalyst retained more than 90% of its ECSA, mass activity and specific activity. This effect was attributed to (i) a partial nitrogen-doping of the carbon surface, acting as anchoring sites for the Pt nanoparticles, and (ii) a higher graphitization degree of the N-HTC support. The increased stability is most probably a combination of the mentioned particle size effects and support effects. As such, N-HTC carbon aerogels are, after fine tuning of their physicochemical properties by pyrolysis, promising supports for the design of supported electrocatalysts.

Experimental Section

Synthetic procedures

All chemicals were used as received. For the synthesis and washing procedures when using deionized water, solely ultra-pure water (resistivity approx. 18.2 MΩ cm at 25 °C, ELGA LabWater) was used. All gases used (Ar, N₂, O₂, N₂/H₂) were of purity grade 5.0 (Sauerstoffwerk Friedrichshafen GmbH).

Synthesis of crude hydrothermal carbon

The nitrogen-doped hydrothermal carbon materials (N-HTC) were synthesized following a procedure reported by White et al.^[35] Glucose (1.5 g) and ovalbumin (0.3 g) were dispersed in water (13.5 mL) in a glass tube, subsequently placed in a Teflon-inlet lined 45 mL steel-autoclave and heated to 180 °C for 4.5 h using a heating furnace. After cooling down to room temperature, the autoclave was removed from the heating furnace, opened and the formed carbonaceous gel-type monolith was isolated and washed in excess first with water and second with ethanol. A subsequent solvent exchange from ethanol to water was performed in order to freeze-dry (-110 °C, 0.1 mbar) the crude product for 24 h to sublimate the solvent, while preserving the filigree coral-like aerogel structure.

Synthesis of carbonized N-HTC materials

In a typical batch size, 200 mg of raw product were put in a ceramic combustion boat (Carl Roth) and then placed in a quartz tube under inert (N₂) atmosphere. Prior to carbonization the atmosphere in the tube was exchanged with N₂ by sequentially applying vacuum and flushing N₂ gas for three times, followed by continuous N₂ purging for 2 h. The samples were then carbonized in a tubular oven (Linn High Therm GmbH) for 4 h (10 K min⁻¹) at 900 and 1000 °C, respectively. To synthesize the sample at 1500 °C, the sample pre-treated at 900 °C was graphitized (1500 °C, 2 h,

5 K min⁻¹) in a glassy carbon crucible (SIGRADUR®, HTW Hochtemperatur-Werkstoffe GmbH) in an Astro-oven (Astro-oven, Thermal Technology Inc.) under a constant Ar flow (50 mL min⁻¹). Sample names are abbreviated as N-HTC-PT, with N-HTC standing for nitrogen-doped hydrothermal carbon and *T* standing for the carbonization or graphitization temperature (*T* = 900/1000 or 1500 °C), respectively.

Synthesis of Platinum/N-HTC materials

The Pt/N-HTC catalysts were prepared by wet impregnation. In a typical experiment N-HTC (20 mg) was suspended in a mixture of deionized H₂O and *i*PrOH (300 μL mg⁻¹, 1:1, v:v) and H₂PtCl₆·6 H₂O (35.4 mg, 0.07 mmol, AlfaAesar, Premion® 99.999%) resulting in a platinum loading of 40 wt%. After mixing with a horn sonicator (40% amplitude, 20 min, Branson) at 0 °C, the sample was freeze-dried (-110 °C, 0.1 mbar) to remove the solvent. The Platinum (IV) precursor was then reduced under N₂/H₂ (10 vol.%) in a tubular oven (Carbolite GmbH) at 100 °C (2 h, 10 K min⁻¹) and afterwards cooled to room temperature under nitrogen atmosphere. Sample names are abbreviated as Pt₄₀/N-HTC-PT, with Pt₄₀ indicating the platinum loading of 40 wt% on the carbon support and *T* indicating the pyrolysis temperature.

Physical characterization

Electron microscopy

Scanning electron microscopy (SEM) micrographs of the prepared Pt/N-HTC materials were recorded with a FEG-HRSEM SU8220 (Hitachi) microscope (20 kV). High-resolution Transmission electron microscopy (TEM) micrographs were recorded with a Talos 200X (ThermoFisher) operated at an acceleration voltage of 200 kV. All measurements were done using copper grids, coated with a thin-film of amorphous carbon on which a small amount of sample was deposited.

N₂ physisorption measurements

Surface area, pore volume and pore size distribution were determined from N₂ physisorption isotherms obtained at 77 K with a Quantachrome Autosorb using the Brunauer-Emmett-Teller (BET) theory and quenched solid density functional theory (QSDFT), respectively.

Elemental composition

The C, N, H, S bulk composition was determined via quantitative sample combustion analysis at 1150 °C with a Vario MICRO Cube system (Elementar Analysensysteme GmbH, Germany).

X-ray photoelectron spectroscopy (XPS)

XPS spectra were acquired with a Thermo Scientific K-alpha+ spectrometer. The samples were analyzed using a microfocused, monochromated Al Kα X-ray source (400 μm spot size). The monochromatic Al Kα line was used as X-ray excitation (1486.6 V) with a pass energy of 50 eV to obtain high resolution spectra. The XPS spectra were fitted with one or more Voigt profiles (with a binding energy uncertainty of ±0.2 eV) and Scofield sensitivity factors were applied for quantification.^[68] All spectra were referenced to the C 1s peak (C-C, C-H) at a binding energy of 285.0 eV. Accuracy of binding energy was thereby controlled by means of

the photoelectron peaks of metallic Cu, Ag, and Au, respectively. In addition carbon (C 1s) spectra were recorded at the beginning and after each analysis, to exclude any sample degradation under irradiation.

Near-edge X-ray absorption fine structure (NEXAFS) spectroscopy

NEXAFS measurements were performed at the He-SGM beamline at BESSYII (Helmholtz-Zentrum Berlin, Germany),^[69] except for N-HTC-P1500 which has been measured at the X-Treme Beamline at the Swiss Light Source (Paul Scherrer Institute, Villigen, Switzerland).^[70] The samples were pressed in Indium-foil and measured in the beam at an angle of incidence of 55° using linearly polarised radiation. C and N K-edge spectra of the samples were measured in partial electron mode at counter voltages of 150 kV and 250 kV, respectively. The effect of carbon contamination at the beamline optics was taken into account by dividing the raw data by a spectrum of a freshly sputtered Au foil. Furthermore, the data were normalized to an edge jump of 1. The sp²-C content of the sample was estimated by comparing the π* peak intensity at 285.6 eV, normalized to the area between 290.5–305 eV, with a 100% sp²-C reference material, i. e. highly ordered pyrolytic graphite (HOPG).

X-ray diffraction (XRD) and Rietveld refinement

The XRD characterization of the N-HTC carbon supports pyrolyzed at different temperatures and of the resulting Pt/N-HTC catalysts were measured in glass capillaries (diameter 0.5 mm, Hilgenberg) in a Debye-Scherrer geometry. Measurements were performed using a STOE diffractometer with a Cu-Kα1 radiation (λ = 0.15417 nm, 40 kV, 30 mA) and a Ge (111) monochromator. The X-ray gun was operated at 40 kV and 30 mA. The diffractograms were recorded from 10° to 106° (2θ) using a step width of 0.5° and a step time of 120 s. For Rietveld refinements the FullProf software (Version 6.30 – Sep2018-ILL JRC) was used.^[71]

Raman microscopy

Raman microscopy measurements were executed with a Senterra II system (Bruker). The Raman spectra were obtained by excitation with a laser (532 nm) operated at approximately 2.5 mW. The detector was a Peltier-cooled charge coupled device camera, and the spectral resolution was set to 4 cm⁻¹. The measurements were performed with a ×50 ULWD objective and a 200 μm confocal aperture. Curve fitting was performed with the software Origin. An accurate fitting of the Raman spectra was done by the consideration of five bands (G-band at ~1580 cm⁻¹, D1-band at ~1345 cm⁻¹, D2-band at ~1604 cm⁻¹, D3-band at ~1530 cm⁻¹ and D4-band at ~1210 cm⁻¹) as described in detail elsewhere.^[52]

Total scattering analysis

Total scattering measurements were performed at the beamline P02.1 at PETRA III, DESY.^[72] Therefore, all samples were filled into soda glass capillaries (Hilgenberg) with a diameter of 0.8 mm and a wall thickness of 0.01 mm. The intensities of the scattered X-rays were detected using a PerkinElmer XRD1621 flat panel detector at a sample detector spacing of 336 mm and an X-ray wavelength of 0.2073 Å. The detector was calibrated using a LaB₆ (NIST 660b) standard. In order to reduce the two-dimensional (2D) images of the scattered X-ray events to one-dimensional (1D) scattered intensity data the DAWN software package^[73] was used. For further data processing the software pdfgetX3^[74] was used. The structure

function $S(Q)$ was obtained from the intensity of the scattered X-rays by subtracting an empty capillary measurement and further corrections for Compton scattering, self-absorption and multiple scattering. The reduced pair distribution function $G(r)$ was generated from $S(Q)$ by Fourier transformation.

Electrical conductivity

The electrical conductivity of the N-HTC supports pyrolyzed at different temperatures was measured in all cases for the same amount of powder (5 mg), which was placed between two freshly polished copper stamps (i. e. after removal of the surface oxide layer) with an area A_{Cu} of 39.7 mm² ($r_{Cu} = 3.55$ mm). Thereby, the thickness t of the pressed powder layer between the stamps was determined to 0.6 mm and 0.38 mm for all applied pressures for the N-HTCs and the Vulcan®XC72R sample, respectively. For various weight loads, 7.5 kg, 14.3 kg and 20.4 kg, corresponding to respective pressures of 1.86 MPa, 3.54 MPa and 5.05 MPa, the resistivity R was determined while applying a current of 1 A between the copper stamps. The electrical conductivity σ then equates to:

$$\sigma = t / (A_{Cu} \cdot R), [\sigma] = S m^{-1} \quad (1)$$

Electrochemical characterization

The electrochemical experiments were carried out with a rotating disk electrode (RDE) setup (636A Rotator, AMETEK SI) operated with a Gamry Interface 1000 potentiostat/galvanostat. In a custom made three-compartment cell, a platinum mesh was used as a counter electrode, a reversible hydrogen electrode (RHE, Hydroflex®, Gaskatel GmbH) was used as reference electrode and the prepared catalyst ink was deposited on a glassy carbon (GC) disk electrode (diameter 5 mm, area_{geo} 0.196 cm²), which serves as working electrode, respectively. The catalyst ink was prepared by dispersing the 40 wt% Pt/N-HTC or carbon catalysts (3.00 mg) in a mixture of deionized H₂O (1990 μL) and *i*PrOH (500 μL). The ionomer Nafion™ (10 μL, 5 wt% solution in a mixture of lower aliphatic alcohols and water, Sigma-Aldrich) was added and the mixture was homogenized with a horn sonicator (40% amplitude, 20 min, Branson) at 0°C. Afterwards the ink (10 μL) was drop-cast on a freshly mirror polished (with alumina polishing solutions, diameter 1.0 and 0.05 μm, Buehler) GC rotating disk electrode and the film was dried in air at room temperature under rotation (400 rpm), resulting in a homogenous thin-film with a platinum loading of $L_{Pt} = 25 \mu g_{Pt} cm_{geo}^{-2}$. All experiments were conducted in freshly prepared 0.1 M HClO₄ (Sigma-Aldrich). The cyclic voltammetry (CV) and accelerated stress test (AST) measurements (carbon support corrosion) were performed in N₂ saturated electrolyte. When saturating with gases (N₂ or O₂, both 5.0) the electrolyte was purged for 30 min and a top-flow during measurements was maintained to avoid any change in gas-saturation. Prior to catalyst ORR testing the catalyst were conditioned by CV from 0.05 to 1 V vs. RHE until a steady state was reached (100 cycles, 100 mV s⁻¹). To determine the electrochemical active surface area (ECSA) another 5 scans at lower scan rates (20 mV s⁻¹) were conducted. The hydrogen underpotential area (H_{UPD}) between 0.09 and 0.40 V vs. RHE was used to calculate the related charge (Q_H) to this process which was then used to calculate the ECSA taking the theoretical value for the adsorption of a hydrogen monolayer on a polycrystalline Pt disk electrode ($Q_H^{theo} = 210 \mu C cm^{-2}$)^[75] and the Pt electrode loading (m_{Pt}) into account:

$$\text{ECSA} = (Q_{\text{H}} / (210 \cdot 10^4 \cdot m_{\text{Pt}})) \cdot 10^{-1}, [\text{ECSA}] = \text{m}^2 \text{g}_{\text{Pt}}^{-1} \quad (2)$$

Afterwards the ORR activity was determined. This was done by recording linear sweep voltammograms (LSV) in O₂ saturated electrolyte. The LSV were performed under rotation at 1600 rpm in an anodic direction (from 0.1 to 1.1 V vs. RHE with 5 mVs⁻¹). For evaluation, recorded background LSV in N₂ saturated electrolyte at the same scanning speed were subtracted from the original measurements. All data were *iR* corrected by measuring the ohmic resistance. The onset potentials for the ORR were determined at the intersection of two applied tangents (0.90 and 1.05 V vs. RHE) from the recorded LSV curves. The mass activities (MA) were determined at 0.9 V vs. RHE, like described elsewhere.^[76]

$$\text{MA} = ((I_{0.9\text{V}} \cdot I_{0.4\text{V}}) / (I_{0.4\text{V}} - I_{0.9\text{V}})) \cdot (1/m_{\text{Pt}}), [\text{MA}] = \text{A mg}_{\text{Pt}}^{-1} \quad (3)$$

When comparing the different catalysts, the activity was also given with regard to the real platinum surface, i.e. the ECSA, determined electrochemically as previously described (*vide supra*). The specific activity (SA) then calculates as follows:

$$\text{SA} = 100 \cdot (\text{MA}/\text{ECSA}), [\text{SA}] = \text{mA cm}_{\text{Pt}}^{-2} \quad (4)$$

The catalyst stability was determined through AST protocols which meet the requirements of the Department of Energy (DoE). For degradation of the carbon support 10,000 cycles from 1.0 to 1.5 V vs. RHE (at 500 mVs⁻¹) were conducted. To determine changes in the ECSA after 10, 100, 1000, 2000, ..., 10,000 cycles, standard CV measurements (*vide supra*) were measured. Before and after the AST measurements the ORR activities were determined, as described before.

Acknowledgements

The authors thank the BMBF for generous funding of the DEKADE (FKZ – 03SF0544D, grantee AF) and TEMCat3D (FKZ – 03SF0590, grantee AF) projects as well as the University of Freiburg for core support funding. In addition, parts of the work were funded by the Deutsche Forschungsgemeinschaft (DFG, German Research Foundation) under Germany's Excellence Strategy (EXC-2193/1-390951807, grantee AF) as well as by the Volkswagen Foundation (Momentum grant, grantee AF). The authors thank the Core Facility 1 (Freiburg Center for Interactive Materials and Bioinspired Technologies, University of Freiburg) for TEM support, as well as Dr. Ralf Thomann and Dr. Yi Thomann for support with the HR-TEM data. The Helmholtz Zentrum Berlin, Germany is acknowledged for the allocation of synchrotron radiation beamtime at the He-SGM Beamline at BESSY II. Further, we thank Dr. Alexei Nefedov for his support in operating the He-SGM Beamline. We acknowledge DESY (Hamburg, Germany), a member of the Helmholtz Association HGF, for the provision of experimental facilities. Part of this research was carried out at PETRA III, Beamline P02.1. We acknowledge the Paul Scherrer Institut, Villigen, Switzerland for provision of synchrotron radiation beamtime at beamline X-Treme of the SLS and would like to thank Dr. Jan Dreiser for sample measurement. XPS was carried out with the support of the Karlsruhe Nano Micro Facility (KNMF, www.knmf.kit.edu), a Helmholtz research infrastructure at Karlsruhe Institute of Technology. The K-Alpha+ instrument was financially supported by the

Federal Ministry of Economics and Technology based on a decision by the German Bundestag. Open Access funding enabled and organized by Projekt DEAL.

Conflict of Interest

The authors declare no conflict of interest.

Keywords: Carbon · Electrochemistry · Fuel Cells · Hydrothermal Synthesis · Platinum

- [1] X. Z. Yuan, H. Wang, in *PEM Fuel Cell Electrocat. Catal. Layers Fundam. Appl.*, Springer London, **2008**, pp. 1–87.
- [2] P. Lang, N. Yuan, Q. Jiang, Y. Zhang, J. Tang, *Energy Technol.* **2020**, *8*, 1900984.
- [3] E. Antolini, *Appl. Catal. B* **2016**, *181*, 298–313.
- [4] F. J. Perez-Alonso, D. N. McCarthy, A. Nierhoff, P. Hernandez-Fernandez, C. Strebler, I. E. L. Stephens, J. H. Nielsen, I. Chorkendorff, *Angew. Chem. Int. Ed.* **2012**, *51*, 4641–4643; *Angew. Chem.* **2012**, *124*, 4719–4721.
- [5] X. Yu, S. Ye, *J. Power Sources* **2007**, *172*, 133–144.
- [6] K. J. J. Mayrhofer, J. C. Meier, S. J. Ashton, G. K. H. Wiberg, F. Kraus, M. Hanzlik, M. Arenz, *Electrochem. Commun.* **2008**, *10*, 1144–1147.
- [7] J. Melke, R. Schuster, S. Möbus, T. Jurzinsky, P. Elsässer, A. Heilemann, A. Fischer, *Carbon* **2019**, *146*, 44–59.
- [8] S. Zhang, T. Fu, J. Li, Y. Peng, J. Zhao, *ACS Appl. Energ. Mater.* **2018**, *1*, 6198–6207.
- [9] K. Kinoshita, *Electrochemical and Physicochemical Properties*, Wiley-VCH, Weinheim, **1988**.
- [10] R. Brandiele, C. Durante, M. Zerbetto, N. Vicentini, T. Kosmala, D. Badocco, P. Pastore, G. A. Rizzi, A. A. Isse, A. Gennaro, *Electrochim. Acta* **2018**, *277*, 287–300.
- [11] Y. Chen, J. Wang, H. Liu, R. Li, X. Sun, S. Ye, S. Knights, *Electrochem. Commun.* **2009**, *11*, 2071–2076.
- [12] S. H. Liu, M. T. Wu, Y. H. Lai, C. C. Chiang, N. Yu, S. Bin Liu, *J. Mater. Chem.* **2011**, *21*, 12489–12496.
- [13] S. Ott, A. Orfanidi, H. Schmies, B. Anke, H. N. Nong, J. Hübner, U. Gernert, M. Glicch, M. Lerch, P. Strasser, *Nat. Mater.* **2020**, *19*, 77–85.
- [14] A. L. Dicks, *J. Power Sources* **2006**, *156*, 128–141.
- [15] Y. J. Wang, D. P. Wilkinson, J. Zhang, *Chem. Rev.* **2011**, *111*, 7625–7651.
- [16] A. Bharti, G. Cheruvaly, *J. Power Sources* **2017**, *360*, 196–205.
- [17] F. Hasché, M. Oezaslan, P. Strasser, *Phys. Chem. Chem. Phys.* **2010**, *12*, 15251–15258.
- [18] Z. Liu, L. M. Gan, L. Hong, W. Chen, J. Y. Lee, *J. Power Sources* **2005**, *139*, 73–78.
- [19] C. A. Bessel, K. Laubernds, N. M. Rodriguez, R. T. K. Baker, *J. Phys. Chem. B* **2001**, *105*, 1121–1122.
- [20] M. Tsuji, M. Kubokawa, R. Yano, N. Miyamae, T. Tsuji, M. S. Jun, S. Hong, S. Lim, S. H. Yoon, I. Mochida, *Langmuir* **2007**, *23*, 387–390.
- [21] N. Job, J. Marie, S. Lambert, S. Berthon-Fabry, P. Achard, *Energy Convers. Manage.* **2008**, *49*, 2461–2470.
- [22] A. Smirnova, X. Dong, H. Hara, A. Vasiliev, N. Sammes, *Int. J. Hydrogen Energy* **2005**, *30*, 149–158.
- [23] Q. Wang, H. Li, L. Chen, X. Huang, *Carbon* **2001**, *39*, 2211–2214.
- [24] M.-M. Titirici, M. Antonietti, N. Baccile, *Green Chem.* **2008**, *10*, 1204.
- [25] X. Sun, Y. Li, *Angew. Chem. Int. Ed.* **2004**, *43*, 597–601; *Angew. Chem.* **2004**, *116*, 607–611.
- [26] M. Bosilj, L. Rustam, R. Thomann, J. Melke, A. Fischer, R. J. White, *Catal. Sci. Technol.* **2020**, *10*, 4794–4808.
- [27] M. Soorholtz, R. J. White, T. Zimmermann, M. M. Titirici, M. Antonietti, R. Palkovits, F. Schüth, *Chem. Commun.* **2013**, *49*, 240–242.
- [28] S. Van Dommele, K. P. De Jong, J. H. Bitter, *Top. Catal.* **2009**, *52*, 1575–1583.
- [29] R. Demir-Cakan, P. Makowski, M. Antonietti, F. Goettmann, M. M. Titirici, *Catal. Today* **2010**, *150*, 115–118.
- [30] C. He, A. Giannis, J. Y. Wang, *Appl. Energy* **2013**, *111*, 257–266.
- [31] X. Zhuang, H. Zhan, Y. Huang, Y. Song, X. Yin, C. Wu, *Bioresour. Technol.* **2018**, *267*, 17–29.
- [32] C. Zhang, X. Ma, X. Chen, Y. Tian, Y. Zhou, X. Lu, T. Huang, *Energy* **2020**, *197*, 117193.

- [33] B. Huang, Y. Liu, Z. Xie, *J. Mater. Chem. A* **2017**, *5*, 23481–23488.
- [34] K. Preuss, L. C. Tañase, C. M. Teodorescu, I. Abrahams, M. M. Titirici, *J. Mater. Chem. A* **2017**, *5*, 16336–16343.
- [35] R. J. White, N. Yoshizawa, M. Antonietti, M. M. Titirici, *Green Chem.* **2011**, *13*, 2428–2434.
- [36] N. Brun, S. A. Wohlgemuth, P. Osiceanu, M. M. Titirici, *Green Chem.* **2013**, *15*, 2514–2524.
- [37] S.-A. Wohlgemuth, T.-P. Fellingner, P. Jäker, M. Antonietti, *J. Mater. Chem. A* **2013**, *1*, 4002.
- [38] J. Melke, J. Martin, M. Bruns, P. Hügenell, A. Schökel, S. Montoya Isaza, F. Fink, P. Elsässer, A. Fischer, *ACS Appl. Energ. Mater.* **2020**, *3*, 11627–11640.
- [39] Y. Zou, A. S. Walton, I. A. Kinloch, R. A. W. Dryfe, *Langmuir* **2016**, *32*, 11448–11455.
- [40] N. Y. Kostina, O. Pop-Georgievski, M. Bachmann, N. Neykova, M. Bruns, J. Michálek, M. Basmeyer, C. Rodriguez-Emmenegger, *Macromol. Biosci.* **2016**, *16*, 83–94.
- [41] S. Tardio, M. L. Abel, R. H. Carr, J. F. Watts, *Surf. Interface Anal.* **2016**, *48*, 556–560.
- [42] J. H. Zhou, Z. J. Sui, J. Zhu, P. Li, D. Chen, Y. C. Dai, W. K. Yuan, *Carbon* **2007**, *45*, 785–796.
- [43] U. Zielke, K. J. Hüttinger, W. P. Hoffman, *Carbon* **1996**, *34*, 983–998.
- [44] R. Arrigo, M. Hävecker, R. Schlögl, D. S. Su, *Chem. Commun.* **2008**, 4891–4893.
- [45] J. R. Pels, F. Kapteijn, J. A. Moulijn, Q. Zhu, K. M. Thomas, *Carbon* **1995**, *33*, 1641–1653.
- [46] J. Melke, P. Jakes, J. Langner, L. Riekehr, U. Kunz, Z. Zhao-Karger, A. Nefedov, H. Sezen, C. Wöll, H. Ehrenberg, C. Roth, *Carbon* **2014**, *78*, 220–230.
- [47] J. Stöhr, *NEXAFS Spectroscopy*, Springer Berlin Heidelberg, Berlin, Heidelberg, **1992**.
- [48] R. A. Rosenberg, P. J. Love, V. Rehn, *Phys. Rev. B* **1986**, *33*, 4034–4037.
- [49] J. P. Boudou, P. Parent, F. Suárez-García, S. Villar-Rodil, A. Martínez-Alonso, J. M. D. Tascón, *Carbon* **2006**, *44*, 2452–2462.
- [50] A. C. Ferrari, J. Robertson, *Phys. Rev. B* **2000**, *61*, 14095–14107.
- [51] M. Pawlyta, J. N. Rouzaud, S. Duber, *Carbon* **2015**, *84*, 479–490.
- [52] A. Sadezky, H. Muckenhuber, H. Grothe, R. Niessner, U. Pöschl, *Carbon* **2005**, *43*, 1731–1742.
- [53] J. Melke, B. Peter, A. Habereeder, J. Ziegler, C. Fasel, A. Nefedov, H. Sezen, C. Wöll, H. Ehrenberg, C. Roth, *ACS Appl. Mater. Interfaces* **2016**, *8*, 82–90.
- [54] M. Oschatz, P. Pré, S. Dörfler, W. Nickel, P. Beaunier, J. N. Rouzaud, C. Fischer, E. Brunner, S. Kaskel, *Carbon* **2016**, *105*, 314–322.
- [55] O. Beyssac, B. Goffé, J. P. Petit, E. Froigneux, M. Moreau, J. N. Rouzaud, *Spectrochim. Acta Part A* **2003**, *59*, 2267–2276.
- [56] J. Sánchez-González, A. Maclás-García, M. F. Alexandre-Franco, V. Gómez-Serrano, *Carbon* **2005**, *43*, 741–747.
- [57] B. Marinho, M. Ghislandi, E. Tkalya, C. E. Koning, G. de With, *Powder Technol.* **2012**, *221*, 351–358.
- [58] U. S. Department of Energy, “Fuel Cell Technologies Office Multi-Year Research, Development, and Demonstration Plan – Section 3.4 Fuel Cells,” can be found under https://www.energy.gov/sites/default/files/2017/05/f34/fcto_myrd_fuel_cells.pdf, **2016**.
- [59] K. Shinozaki, Y. Morimoto, B. S. Pivovar, S. S. Kocha, *Electrochim. Acta* **2016**, *213*, 783–790.
- [60] Y. Zhou, R. Pasquarelli, T. Holme, J. Berry, D. Ginley, R. O’Hayre, *J. Mater. Chem.* **2009**, *19*, 7830–7838.
- [61] Y. Zhou, K. Neyerlin, T. S. Olson, S. Pylypenko, J. Bult, H. N. Dinh, T. Gennett, Z. Shao, R. O’Hayre, *Energy Environ. Sci.* **2010**, *3*, 1437–1446.
- [62] L. Perini, C. Durante, M. Favaro, V. Perazzolo, S. Agnoli, O. Schneider, G. Granozzi, A. Gennaro, *ACS Appl. Mater. Interfaces* **2015**, *7*, 1170–1179.
- [63] C. Hung, P. Lim, J. Chen, H. C. Shih, *J. Power Sources* **2011**, *196*, 140–146.
- [64] X. Zhao, A. Hayashi, Z. Noda, I. Yagi, K. Sasaki, *Electrochim. Acta* **2013**, *97*, 33–41.
- [65] P. Jovanovič, A. Pavličič, V. S. Šelih, M. Šala, N. Hodnik, M. Bele, S. Hočevar, M. Gaberšček, *ChemCatChem* **2014**, *6*, 449–453.
- [66] E. F. Holby, W. Sheng, Y. Shao-Horn, D. Morgan, *Energy Environ. Sci.* **2009**, *2*, 865–871.
- [67] R. L. Borup, A. Kusoglu, K. C. Neyerlin, R. Mukundan, R. K. Ahluwalia, D. A. Cullen, K. L. More, A. Z. Weber, D. J. Myers, *Curr. Opin. Electrochem.* **2020**, *21*, 192–200.
- [68] J. H. Scofield, *J. Electron Spectrosc. Relat. Phenom.* **1976**, *8*, 129–137.
- [69] A. Nefedov, C. Wöll, *Springer Ser. Surf. Sci.* **2013**, *51*, 277–303.
- [70] C. Piamonteze, U. Flechsig, S. Rusponi, J. Dreiser, J. Heidler, M. Schmidt, R. Wetter, M. Calvi, T. Schmidt, H. Pruchova, J. Krempasky, C. Quitmann, H. Brune, F. Nolting, *J. Synchrotron Radiat.* **2012**, *19*, 661–674.
- [71] J. Rodríguez-Carvajal, *Phys. Condens. Matter* **1993**, *192*, 55–69.
- [72] A.-C. Dippel, H.-P. Liermann, J. T. Delitz, P. Walter, H. Schulte-Schrepping, O. H. Seeck, H. Franz, *J. Synchrotron Radiat.* **2015**, *22*, 675–687.
- [73] J. Filik, A. W. Ashton, P. C. Y. Chang, P. A. Chater, S. J. Day, M. Drakopoulos, M. W. Gerring, M. L. Hart, O. V. Magdysyuk, S. Michalik, A. Smith, C. C. Tang, N. J. Terrill, M. T. Wharmby, H. Wilhelm, *J. Appl. Cryst.* **2017**, *50*, 959–966.
- [74] P. Juhás, T. Davis, C. L. Farrow, S. J. L. Billinge, *J. Appl. Cryst.* **2013**, *46*, 560–566.
- [75] K. Shinozaki, J. W. Zack, R. M. Richards, B. S. Pivovar, S. S. Kocha, *J. Electrochem. Soc.* **2015**, *162*, F1144–F1158.
- [76] T. J. Schmidt, H. A. Gasteiger, in *Handb. Fuel Cells*, John Wiley & Sons, Ltd, Chichester, UK, **2010**.

Manuscript received: August 27, 2021

Revised manuscript received: November 8, 2021

Accepted manuscript online: November 14, 2021